Check for updates

Modulation of lithium-ion transport kinetics in polymer-based electrolytes by defect engineering for ultralong-cycling solid-state lithium metal batteries

Yunpeng Qu,[a] Lin Wang,[a] Changxing Han,[a] Borui Li,[a] Wenkai Song,[a] Chang Su,[a] Wanyuan Jiang,[b] Dongming Liu,[a] Mengfan Pei,[a] Xin Jin,[a] Shuo Zhuo,[a] Runyang Li,[a] Jinfeng Zhang,[a] Xigao Jian [ID] *[a,b] and Fangyuan Hu [ID] *[a]

Solid-state lithium metal batteries (SSLMBs) have emerged with great promise in the field of next-generation battery technology, owing to the inherent safety and energy density benefits. However, there is an urgent need to address the core bottlenecks of slow ion migration and the unstable electrode/electrolyte interface in polymer electrolytes for their development. Herein, a composite polymer electrolyte (PHMS) is constructed by introducing sulfur vacancy-enriched 2D MoS_x nanosheets into a poly(vinylidene fluoride-*co*-hexafluoropropylene) (PVDF-HFP) matrix through a defect engineering strategy, which is employed to simultaneously optimise lithium ion transport kinetics and construct a stable interface. Theoretical calculations and experiments have confirmed that MoS_x significantly promotes the dissociation of lithium salts and induces the conversion of polymers to the high-dielectric β-phase to form high-speed ion channels. Furthermore, synchronous triggering of the *in situ* reaction with lithium metal can generate a heterogeneous solid electrolyte interface (SEI) layer containing LiF/lithium–molybdenum compounds, which enhances the long-term operational stability of the battery. Consequently, a stable cycling capacity of 8500 cycles at 8C multiplicity can be obtained for the LFP|PHMS|Li cell, with a single-cycle decay rate of a mere 0.002%, and the pouch cell also exhibits considerable practical potential. This study proposes a novel approach for designing a polymer electrolyte for the development of long-life and high-safety solid-state batteries.

Broader context

The demand for next-generation energy storage systems that combine safety and high energy density has resulted in solid-state lithium metal batteries being propelled to the forefront of key technologies. While polymer electrolytes offer certain advantages in terms of processing, their practical application has been hindered by two interconnected issues: poor ionic conductivity and an unstable, dynamically changing interface with lithium metal. Existing modification strategies generally address these issues in isolation. This study deviates from the conventional approach by utilizing molybdenum disulphide (MoS_x) nanosheets with sulphur-rich vacancies as functional nanofillers to simultaneously optimize bulk ionic transport kinetics and electrode/electrolyte interface stability. The intrinsic vacancies in MoS_x act as active sites, promoting lithium salt dissociation and inducing the formation of a high-dielectric polymer matrix, thereby constructing fast ion transport channels. Concurrently, these defects facilitate the formation of a unique composite solid electrolyte interface (SEI) that is rich in LiF, thereby providing effective protection for the lithium anode. This comprehensive strategy, which employs defect engineering methodologies to address both internal and interface-related challenges, achieves long-term cycling stability at elevated rates, pointing the way forward for the development of durable solid-state batteries.

[a]*School of Materials Science and Engineering, State Key Laboratory of Fine Chemicals, Frontiers Science Center for Smart Materials Oriented Chemical Engineering, Technology Innovation Center of High Performance Resin Materials (Liaoning Province), Dalian University of Technology, Dalian 116024, China. E-mail: jian4616@dlut.edu.cn, hufangyuan@dlut.edu.cn*
[b]*State Key Laboratory of Fine Chemicals, Frontiers Science Center for Smart Materials Oriented Chemical Engineering, School of Chemical Engineering, Technology Innovation Center of High Performance Resin Materials (Liaoning Province), Dalian University of Technology, Dalian 116024, China*

Introduction

In light of the rapid advancements being made in high-energy-density and high-safety energy storage devices, solid-state lithium metal batteries (SSLMBs) have become the primary focus of contemporary battery technology on account of their inherent safety and energy-density advantages.[1,2] Solid-state electrolytes (SSEs), a pivotal component for replacing flam-

mable liquid electrolytes, must possess not only considerable mechanical strength, but also an extensive electrochemical window to ensure compatibility with high-voltage cathode materials.[3] Concurrently, SSEs are required to effectively curtail the proliferation of lithium dendrites.[4,5] Inorganic sulfide or oxide solid-state electrolytes have been shown to exhibit high levels of ionic conductivity. However, their inherent brittleness, large electrode/electrolyte interfacial impedance, and complex processing have been identified as factors that hinder their practical applications.[6–8] In contrast, polymer solid-state electrolytes (SPEs) are distinguished by their exceptional flexibility, favourable interfacial compatibility, and well-established, straightforward processing methods, which suggests unique application prospects.[9–11]

Among the extensive array of polymer matrices, poly(ethylene oxide) (PEO)-based electrolytes have been the subject of considerable research due to their favorable compatibility with lithium salts. However, their limited room-temperature ionic conductivity and deficient antioxidant capacity impose substantial constraints on the energy density and rate performance of batteries.[12,13] Conversely, poly(vinylidene fluoride) (PVDF)-based systems are regarded as optimal polymer carriers for the fabrication of room-temperature high-performance solid-state batteries, a consequence of their elevated dielectric constants, reduced crystallinity, as well as exceptional thermal stability and mechanical properties.[14–16] Nevertheless, PVDF-based electrolytes continue to encounter numerous challenges. For instance, the separation of the polymer and solvent phases gives rise to an internal porous structure, which in turn triggers uneven ion fluxes and localized current density concentration, thereby accelerating the growth of lithium dendrites.[17–19] In addition, the room-temperature ionic conductivity and lithium-ion mobility of the material have certain limitations. This slows down lithium ion transport kinetics in the electrolyte and causes a significant increase in concentration polarization.[20–22] Furthermore, residual solvent molecules continue to undergo side reactions at the interface, irreversibly depleting the active lithium and forming an unstable solid electrolyte interface (SEI).[23,24] In recent years, the design of fillers has yielded novel concepts for high-performance PVDF-based electrolytes, with the optimization of the electrolyte structure through chemical interactions being a key development.[25–27] However, the effect of synergistic regulatory mechanisms of functional fillers on ion transport kinetics and interfacial stability remains to be elucidated, and conventional composite electrolytes continue to be challenging to meet the stringent requirements of SSLMBs for long cycle life and high rate performance.[28,29]

Herein, a polymer-based solid-state electrolyte was designed on the basis of a defect-engineered filler design, with the objective of constructing a compact and homogeneous composite electrolyte with high-flux lithium ion transport. To this end, 2D MoS_x nanosheets enriched with defects, such as sulfur vacancies (S-Vs), were introduced into a poly(vinylidene fluoride-co-hexafluoropropylene) (PVDF-HFP) matrix (PHMS) (Scheme 1). The incorporation of MoS_x fillers promoted the dissociation of lithium salts, resulting in an increased release of more free lithium ions. In addition, defect-induced strong polar interactions broke the symmetry of the polymer chains, consequently inducing the transformation of the non-polar α-phase into the high-dielectric β-phase, which also resulted in the formation of an extensive ion-conducting interface within the electrolyte. This enhanced the lithium-ion transport kinetics, with the exchange current density rising to 0.61 mA cm^{-2}. Synchronously, the formation of such defects also plays a pivotal role in promoting the decomposition of anions, homogenizing the ionic flow at the interface and forming an inorganic-rich SEI, which provides effective protection for the lithium anode. The *in situ* reaction between MoS_x and the lithium metal anode also resulted in the generation of charac-
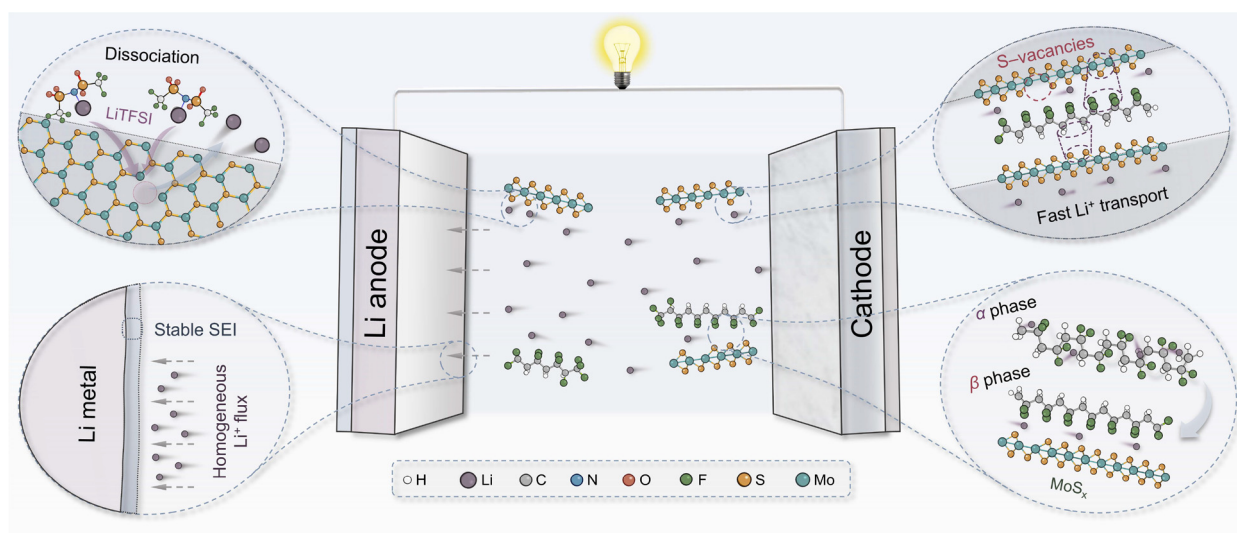
Scheme 1 Schematic diagram and the functions of MoS_x nano-fillers in the PHMS electrolyte.

teristic lithium–molybdenum compound fractions in the SEI, thereby facilitating the uniform distribution and deposition of lithium ions, as well as effectively suppressing the generation of lithium dendrites. Thanks to the efficient lithium ion transport and excellent interfacial stability, the LFP|PHMS|Li cell can maintain stable cycling for 8500 cycles at a high current density of 8C with an average capacity decay rate of merely 0.002% per cycle, and it also demonstrates practical application potential in pouch cells. This work provides a practical and innovative strategy for the design of SPE materials for ultralong-life solid-state batteries.

Results and discussion

Design strategy of PHMS and optimization of Li$^+$ transport behavior

The synthesis of MoS$_x$ containing vacancy defects was accomplished through a high-energy ball milling process, subsequently followed by annealing in an argon atmosphere. As shown in Fig. S1, the results of high-resolution transmission electron microscopy (HRTEM) demonstrate that the treated MoS$_x$ still exhibits a typical lamellar structure. This configuration serves to augment the contact interface between the filler and the polymer matrix, as well as the lithium salt, thereby providing a greater number of active sites for ion transport.[30] The presence of irregular lattice stripes within the region is attributed to intrinsic defects formed in MoS$_x$. The crystal phases of MoS$_x$ and MoS$_2$ were analyzed by X-ray diffraction (XRD) (Fig. S2). The diffraction peaks of both materials corresponded to the standard diffraction pattern (PDF#37-1492),

thus proving the consistency of the phases. However, it was found that defects had been introduced, resulting in changes in the peak intensity and the half-peak width of MoS$_x$. In order to further illustrate the formation of defects in depth, the structure of MoS$_x$ was meticulously observed using spherical aberration-corrected transmission electron microscopy (AC-TEM) (Fig. 1a), where it can be clearly seen that the absence of atoms and the formation of irregular defects occurred at the edges of the lamellae of MoS$_x$ nanosheets and that the crystallographic spacing of 2.50 Å corresponded to the (012) crystallographic surface of MoS$_x$. As demonstrated in Fig. 1b, the characterization of the sulfur vacancies (S-Vs) was confirmed by electron paramagnetic resonance (EPR) spectroscopy analysis, wherein tests exhibited an unpaired electronic signal for MoS$_x$ at a g-value of 2.001, emanating from a paramagnetic defect in the S-Vs.[31,32] Furthermore, Raman spectroscopy tests were conducted on MoS$_x$ and MoS$_2$ (Fig. S3), and both exhibited two peaks within the 330–450 cm^{-1} range. The A$_{1g}$ peak at 406.1 cm^{-1} for MoS$_x$ was blue-shifted in comparison with that of MoS$_2$ (404.3 cm^{-1}), suggesting the occurrence of electronic doping in MoS$_2$ due to the creation of S-Vs, thereby strengthening Li$^+$ adsorption. In the E$_{2g}$ mode, MoS$_x$ was similarly blue-shifted by approximately 1.9 cm^{-1}, suggesting that in-plane tensile strain was also produced.[33,34] The outcomes of the Raman spectroscopy analysis also provide strong confirmation of the occurrence of additional defects in the material.

The interaction of defective MoS$_x$ with lithium bis(trifluoromethanesulfonyl)imide (LiTFSI) was investigated by density functional theory (DFT) calculations in order to elucidate its mechanism of promoting the dissociation of LiTFSI and
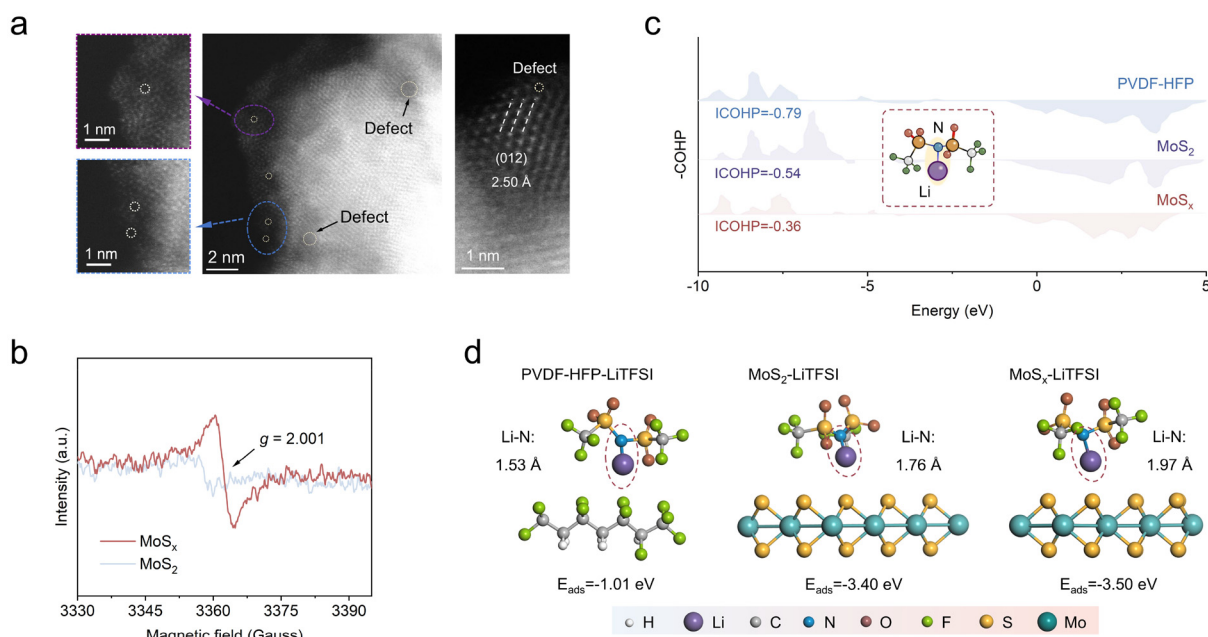

Fig. 1 (a) AC-TEM images of MoS$_x$. (b) EPR spectra of MoS$_x$ and MoS$_2$. (c and d) LiTFSI simulations of the interactions with PVDF-HFP, MoS$_2$, and MoS$_x$ as well as Li−N bond lengths and their integrated crystal orbital Hamiltonian population analysis.

lithium ion transport. As shown in Fig. 1d, the 2D inorganic nanofillers exhibited superior adsorption capabilities for LiTFSI compared to the polymer chain segments of PVDF-HFP, particularly MoS_x with electrophilic S–V centers, which function as active sites for LiTFSI decomposition, demonstrating the highest adsorption energy. The strong adsorption of lithium ions by MoS_x also results in a significant increase in the length of the Li–N bond in LiTFSI, which in turn promotes bond breaking and dissociation of the lithium salt.[26] In order to further investigate the strength of the Li–N bond in LiTFSI, the integrated crystal orbital Hamilton population (iCOHP) of Li–N bonds was analyzed under three conditions (Fig. 1c). The findings demonstrated that the maximum iCOHP values of Li–N bonds were observed in PVDF-HFP, followed by MoS_2 and the lowest in MoS_x. This finding suggests that the coupling of Li–N bonds is weakened by the influence of MoS_x, thereby enhancing the dissociation of LiTFSI.[25,26,35,36]

Therefore, MoS_x was incorporated into the PVDF-HFP-based SPE at the optimized ratio, and the PHMS membrane was fabricated by means of the conventional solution-casting method (Fig. 2a and Fig. S4). The prepared PHMS membranes exhibited a smooth and flat surface, accompanied by commendable flexibility and foldability. Further analysis *via* X-ray microscopy computed tomography (XRM-CT) was conducted in order to reveal the microstructure of the PHMS membrane (Fig. 2a and Fig. S5). The 3D reconstructed images and the corresponding 2D cross-sectional images indicated that the PHMS membrane was both homogeneous and compact, with no serious crack defects. Scanning electron microscopy (SEM) images (Fig. S6a and b) demonstrate the PHMS membrane and the PVDF-HFP composite LiTFSI electrolyte membrane (PHE) without the

added MoS_x filler.[37] Evidently, the structure of PHMS is more uniform and compact than that of PHE, with a smoother membrane surface, which indicates that the incorporation of MoS_x nanofillers fundamentally optimizes the film-formation process. In Fig. S7a–c, the cross-sectional morphology of the two electrolyte membranes is presented, with the lower thickness of the PHMS evident. The corresponding energy-dispersive spectroscopy (EDS) results (Fig. S7b) show a highly homogeneous distribution of the elements Mo, S, C, N, and F, suggesting that MoS_x and lithium salts are uniformly dispersed throughout the 3D polymer network, thus ensuring the efficient transport of ions in the electrolyte.

In practice, the mechanical strength of the material is also a key indicator of the stable application of electrolyte membranes.[38] As shown in Fig. S8, the tensile test of various electrolyte films further substantiates that the incorporation of MoS_x enhances the mechanical strength of the PHMS electrolyte film, with the strain value increasing to 5.85 MPa, which is superior to that of PHE. The excellent mechanical strength can effectively inhibit the growth of lithium dendrites, thereby preventing their penetration of the electrolyte film and averting the occurrence of battery short circuits, as well as maintaining exceptional interfacial compatibility. In addition, further analysis of the thermal stability of the electrolyte was conducted using thermogravimetric analysis (TGA) (Fig. S9). PHMS exhibits a reduced thermal weight loss and an elevated residual carbon rate in comparison with PHE, which suggests that PHMS possesses exceptional thermal stability, while concurrently yielding a lower quantity of residual dimethylformamide (DMF) solvent. Fourier transform infrared spectroscopy (FT-IR) tests confirmed that the residual DMF molecules were co-
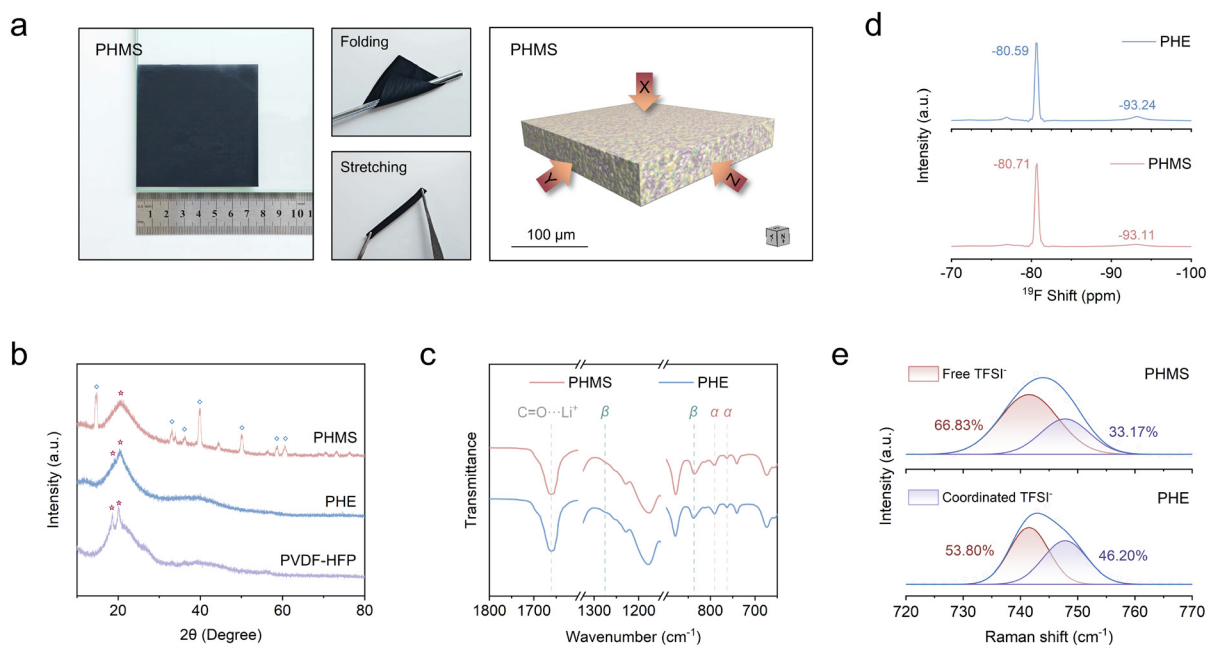

Fig. 2 (a) Optical images of PHMS electrolyte membranes and the corresponding XRM-CT images. (b) XRD analysis of PHMS, PHE and PVDF-HFP. (c) FT-IR spectra of PHMS and PHE. (d) ^{19}F solid-state NMR analysis of PHMS and PHE. (e) Raman spectra of PHMS and PHE.

ordinated with lithium ions (Fig. S10), facilitating lithium salt dissociation and regulating lithium ion transport, which, in turn, enhanced the interfacial stability and electrochemical performance of the electrolyte.

XRD tests were carried out for PHMS and PHE, respectively, as shown in Fig. 2b. The addition of MoS_x resulted in a substantial alteration of the crystalline behavior of PVDF-HFP, characterized by a decline in the degree of crystallinity and an augmentation in the proportion of α-phase (non-polar) to β-phase (polar) transformations in PHMS. The β-phase became the predominant component of the crystalline pattern, which creates a continuous, extensive high-speed ionic transport network throughout the electrolyte, thereby shortening the ion transport path and accelerating the lithium ion transport kinetics.[14,25] Such a phase transition can also be observed from FT-IR tests (Fig. 2c). In order to further characterize the ionic local environment inside the electrolyte, ^{19}F solid-state NMR tests were also performed on different electrolytes, as illustrated in Fig. 2d. In comparison with PHE, the characteristic peak of the PVDF main chain ($-CF_2-$) in PHMS was observed to shift to a lower field, from −93.24 ppm (PHE) to −93.11 ppm (PHMS), which could be attributed to the formation of Li···F–C coordination between dissociated Li^+ and F. Furthermore, the peak representing $TFSI^-$ in PHMS underwent a high-field shift to −80.71 ppm, indicating an increase in free-moving anions in the electrolyte.[39] The degree of dissociation of the lithium salts was analyzed visually using Raman spectroscopy (Fig. 2e). The twin peaks at 741.5 cm^{-1} and 747.8 cm^{-1} represent the fully dissociated unliganded $TFSI^-$ as well as the clusters of liganded ions, respectively.[39,40] The percentage of $TFSI^-$ ions in the electrolyte that did not undergo coordination could be calculated from the different peak areas after fitting. The results demonstrated that the percentage of unliganded $TFSI^-$ increased from 53.80% in PHE to 66.83% in PHMS. The *all-trans* phase transition of the polymer chain segments, in conjunction with the increase of lithium salt dissociation, optimises the lithium ion transport within the electrolyte bulk phase, thereby improving its electrochemical performance.

Basic electrochemical performance of PHMS

In order to verify the regulation of lithium ion transport behavior in PHMS, the lithium ion transference number (t_{Li^+}) was tested. As demonstrated in Fig. 3a and Fig. S11, the Li^+ transference number in PHMS was found to be significantly enhanced in comparison with that of PHE, with t_{Li^+} increasing from 0.16 to 0.63. This enhancement has the potential to reduce the concentration polarization during the processes of battery charging and discharging. It is notable that this rapid lithium ion migration process within the bulk phase results in higher ionic conductivity (σ) and lower ion transport activation energy (E_a) (Fig. 3b and Fig. S12). At a temperature of 30 °C, the increase in ionic conductivity to 0.67 mS cm^{-1} was observed, accompanied by a reduction in activation energy by almost half. As illustrated in Fig. 3c, the Tafel curves show a substantial enhancement in the exchange current density of

PHMS, reaching 0.61 mA cm^{-2}. This value is notably higher than that of PHE, which stands at 0.27 mA cm^{-2}. The results indicate that the modification strategy of PHMS has a significant effect on the energy barrier for the lithium ion migration, accelerating the transport kinetics of Li^+ within the bulk phase and at the interface.[41]

Symmetric Li cells were assembled and subsequently subjected to constant-current charge/discharge (GCD) tests at room temperature, which were used to compare the stability of different electrolytes against the lithium metal anode. The Li|PHMS|Li cell exhibited smooth voltage distributions over an operating time of more than 1800 h (Fig. 3d), indicating that a stable electrode/electrolyte interface was constructed and maintained. Conversely, following 460 h of cycling, the Li|PHE|Li cell exhibited substantial voltage fluctuations, which culminated in a short-circuit failure of the cell. This phenomenon of instability is attributed to the deterioration of the interface, coupled with uncontrolled growth of lithium dendrites. Furthermore, the critical current density (CCD) values of different electrolytes were determined in order to assess their ability to tolerate high current densities without short-circuiting (Fig. 3e). The incorporation of MoS_x resulted in an enhancement of the CCD from 0.6 mA cm^{-2} to 1.1 mA cm^{-2}, thereby substantiating the substantial benefits of PHMS in augmenting interfacial stability and impeding the formation of lithium dendrites.[5,25] This renders it adaptable to elevated rate charging and discharging requirements.

As demonstrated in Fig. 3f, Li||carbon-coated aluminum foil cells were constructed for linear scanning voltammetry (LSV) tests to evaluate the electrochemical stability window of the electrolyte. Compared to PHE, PHMS exhibits a higher oxidative decomposition potential (4.86 V). The electrochemical stability exhibited by PHMS is of paramount importance in order to ensure its compatibility with high-voltage cathode materials, a prerequisite for the successful development of high energy density LMBs. Finally, the reversibility of lithium deposition/stripping on copper foil was evaluated by Li||Cu half-cell tests (Fig. 3g and Fig. S13a, b). The results show that the PHMS system exhibits a higher average coulombic efficiency (CE) and superior cycling stability during the deposition/stripping process. The CE remained at 96.75% after 200 stable cycles at 0.5 mA cm^{-2}, further validating its ability to promote uniform lithium deposition and stabilize SEI formation at the Li metal anode interface.

Stable SEI formation and characterization of the interface

The lithium metal surface post electroplating was subjected to atomic force microscopy (AFM) testing (Fig. 4a–c). The surface of the lithium anode circulating within the PHE system exhibited a substantially elevated structure, and the 3D height profile demonstrated the pronounced growth of irregular dendrites, which resulted in substantial roughening of the surface ($R_a = 61.8$ nm). In contrast, the lithium metal surface after cycling within the PHMS system exhibits a continuous and compact deposition layer, with no obvious dendritic structures, and the surface roughness is significantly reduced to
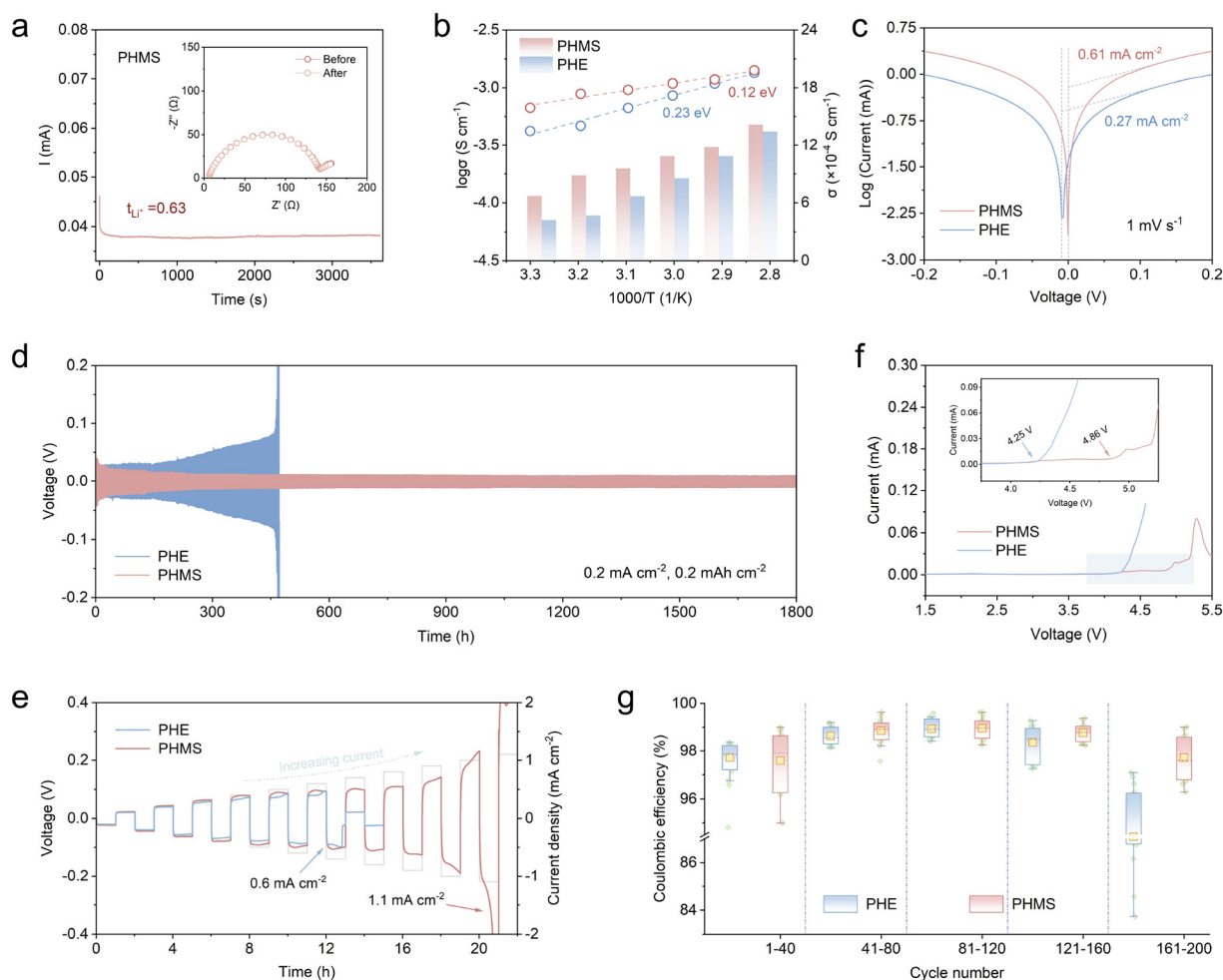
Fig. 3 (a) The Li$^+$ transference number test of PHMS. (b) The temperature-dependent ionic conductivity of PHMS and PHE. (c) Tafel curves of PHMS and PHE. (d) The cycling performance of different symmetric Li cells. (e) CCD tests of PHMS and PHE. (f) LSV tests of various electrolytes. (g) The cycling performance of different Li‖Cu cells at 0.5 mAh cm^{-2}.

28.6 nm, which is 53.7% lower than that in the PHE system. The results presented illustrate the compact and uniform deposition of Li$^+$ on the lithium metal surface in the PHMS system, which serves to fundamentally suppress the risk of dendrite-induced short circuits (Fig. S14 and S15).

The significant discrepancy in the interfacial morphology is directly related to the chemical properties of the SEI. Therefore, the microstructure and compositional evolution of the SEI after cycling were examined using cryo-transmission electron microscopy (Cryo-TEM) and HRTEM. As shown in Fig. 4d and Fig. S16, S17, the SEI layer formed in the PHMS system exhibits distinct and orderly lattice stripes, which are verified to be the co-lattice structure of LiF and Li$_2$O crystalline planes through fast Fourier transform (FFT) analysis. These high-modulus inorganic crystalline phases are interlaced in the interfacial layer to form a continuous and compact passivation layer, which provides a uniform diffusion channel for lithium ions and, at the same time, imparts excellent mechanical strength to the SEI. In order to analyze the SEI composition in more depth, the surface composition of the lithium metal

anode after cycling in PHMS and PHE electrolytes was characterized using X-ray photoelectron spectroscopy (XPS),[42,43] as shown in Fig. 4e. In comparison with PHE, a greater number of LiF components were generated on the lithium surface in the PHMS system, which significantly improved the interfacial stability of the anode. Depth profiling also confirmed the homogeneity of the SEI in the PHMS system over the entire range of interfacial depths with increasing sputtering time (Fig. 4f, g and Fig. S18, S19).

Furthermore, time-of-flight secondary ion mass spectrometry (ToF-SIMS) was employed on sputtered secondary ion fragments on lithium anodes, with the objective of visualizing the distribution of the SEI at varying depth conditions. Fig. 4h shows that the LiF$^-$ signal intensity consistently dominates among all sputtered ion fragments for the PHMS sample, and its intensity gradually stabilizes with increasing sputtering depth. It is worth noting that LiMo$^-$ ions, which represent the characteristic components of LiMo compounds, appear in the fragments, which originate from the *in situ* reaction between the MoS$_x$ filler in the electrolyte and Li during the charging
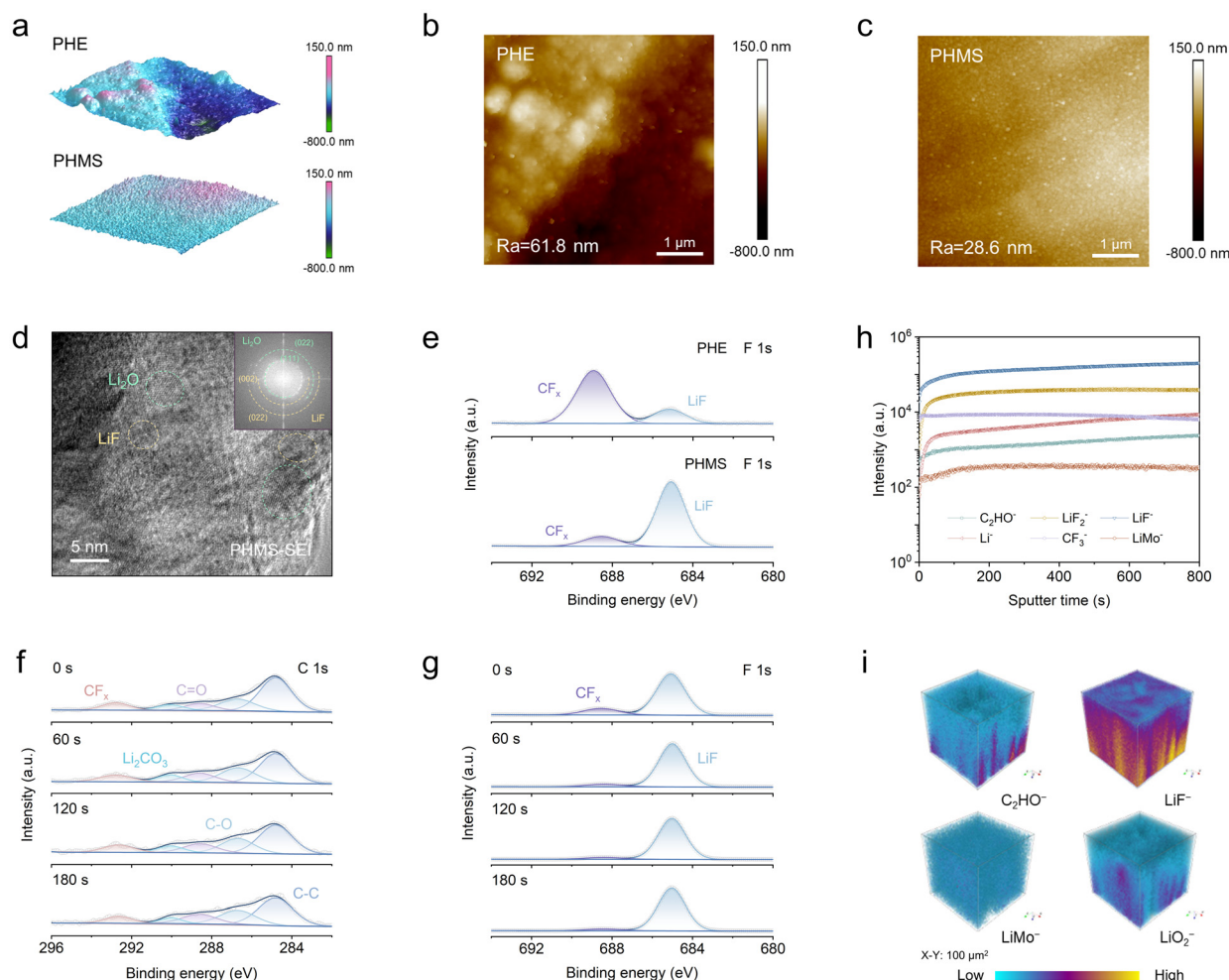
Fig. 4 (a) The 3D AFM images of post-electroplating lithium metal surfaces. (b and c) The corresponding 2D AFM images. (d) Cryo-TEM image and the corresponding FFT analyses for the PHMS-SEI. (e) The surface composition of the lithium anode after cycling in PHMS and PHE electrolytes. (f and g) C 1s and F 1s spectra of the Li anode after cycling in the PHMS electrolyte. (h and i) ToF-SIMS analysis.

and discharging process. The formation of a variety of inorganic components together with the LiF-rich matrix constitutes a composite SEI that is 'rigid–flexible'. The 3D images of ToF-SIMS for different samples are shown in Fig. 4i and Fig. S20, demonstrating that the PHMS system has formed a more homogeneous hybrid SEI compared to PHE, and the 2D cross-sectional depth images also confirm the uniform presence of each inorganic component in the inner layers of the SEI at high concentration (Fig. S21), which ensures long-term stability of the cell.[44]

Electrochemical performance of PHMS-based full cells

To demonstrate the excellent electrochemical performance of the PHMS electrolyte, a systematic evaluation of the electrochemical performance of LFP‖Li cells based on PHMS and PHE electrolytes was conducted. The rate capacity results of LFP|PHMS|Li and LFP|PHE|Li cells at room temperature (1C = 170 mA g^{-1}) are shown in Fig. 5a and Fig. S22a, b. The reversible specific capacities of the PHMS cells were determined to be 159.1, 155.6, 148.2, 137.8, 124.1, and 98.1 mAh g^{-1} at 0.1,

0.2, 0.5, 1, 2, and 5C. Upon the restoration of the current to 0.2C, the reversible capacity was restored to 152.4 mAh g^{-1}, thereby demonstrating satisfactory reversibility. In comparison, the discharge capacities of PHE were only 134.5, 132.7, 125.1, 114.4, 99.9, and 73.0 mAh g^{-1}, which are considerably lower than those of PHMS. Polarization voltage is a significant reflective parameter of interfacial reaction kinetics.[38] As demonstrated in Fig. 5b, the overpotential of PHMS is considerably lower than that of PHE cells at varying currents, and the polarization voltage remains minimal even at 5C. This suggests that PHMS can facilitate lithium ion transportation in an orderly manner under high-current conditions, thereby effectively promoting faster interfacial ion transport kinetics. To further evaluate the long-term cycling stability of the batteries, the cycling performance of each cell was tested at a current density of 2C (Fig. 5c and Fig. S23). The corresponding GCD curves are shown in Fig. 5d and Fig. S24. Following 900 cycles, the PHMS exhibited a specific capacity of 98.1 mAh g^{-1} and a retention rate of 80.7%, indicative of its remarkably stable cycling capability. In contrast, the capacity retention
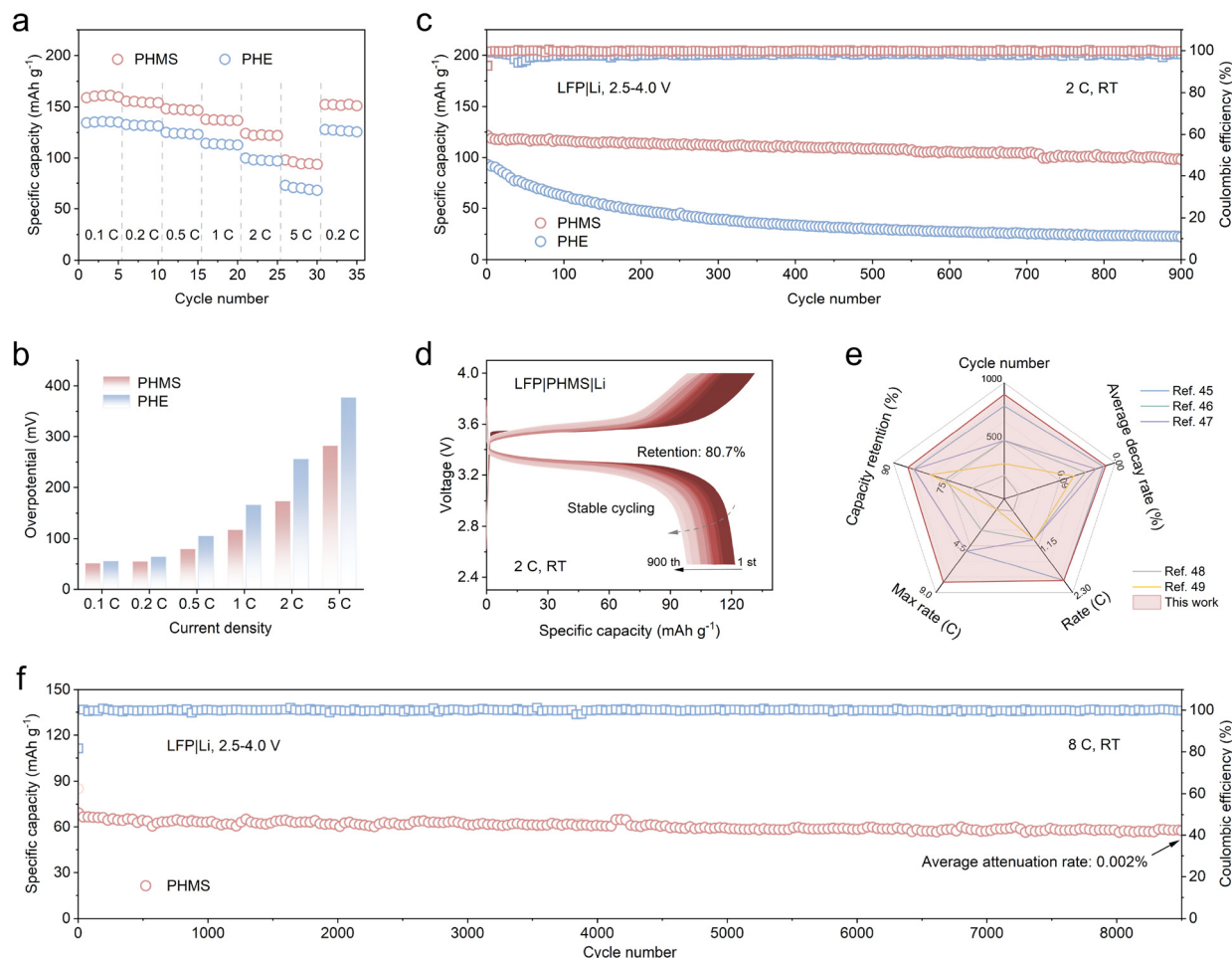
Fig. 5 (a) Rate performance of LFP‖Li cells. (b) Overpotential of LFP‖Li cells at various rates. (c) Cycling performance of LFP‖Li cells at 2C. (d) GCD profiles of PHMS at 2C. (e) The performance comparisons of the LFP|PHMS|Li cell between this work and previously reported work. (f) Cycling performance of the LFP|PHMS|Li cell at 8C.

rates of $PHMoS_2$ and PHE were merely 28.5% and 23.8%, which were considerably lower than that of PHMS. A comparative analysis of analogous polymer electrolytes from disparate perspectives reveals that the combined electrochemical performance of PHMS is significantly superior to that of many previously reported studies (Fig. 5e).[45–49] Moreover, it is notable that the PHMS retains its excellent cycling capability at higher current densities (Fig. 5f). The LFP|PHMS|Li cell demonstrated consistent cycling stability, maintaining 8500 cycles at 8C with an average capacity decay rate of merely 0.002% per cycle, which was compelling evidence of its remarkable ultra-long cycling durability and excellent kinetic stability.

In order to verify the compatibility of the PHMS electrolyte with high-voltage cathode materials in a systematic manner, the electrolytes were matched with the NCM811 cathode, and cycling tests were performed within a voltage window of 2.8–4.3 V. As shown in Fig. 6a, the cycling performance of NCM811|PHMS|Li and NCM811|PHE|Li cells was examined at a current density of 1C (1C = 188 mA g^{-1}). Following 200

cycles, the capacity retention rate of PHMS is 79.7%, while that of PHE is significantly reduced to 10.5%. This is indicative of the substantial enhancement of cycling stability in the high-voltage regime by PHMS. The corresponding GCD curves are presented in Fig. S25. Moreover, electrochemical impedance spectroscopy (EIS) tests were performed on PHMS and PHE cells (Fig. 6b). Due to the better interfacial interactions between the electrolyte and electrodes and the more stable formation of the SEI film, EIS tests show that PHMS has a smaller impedance value than PHE. Notably, when the charging cut-off voltage of the battery was further increased to 4.5 V, as shown in Fig. 6c, the PHMS cell was still able to maintain stable charging and discharging behaviors, verifying its excellent high-voltage tolerance and high-current compatibility.

However, in practical applications, it is also crucial to improve the battery's practical suitability for diverse working conditions. The LFP|PHMS|Li pouch cell was assembled and charged to a fully charged state, after which it was left to stand for 12 h (Fig. S26). In situations involving severe deformation, such as bending, folding, extrusion and puncture, the pouch
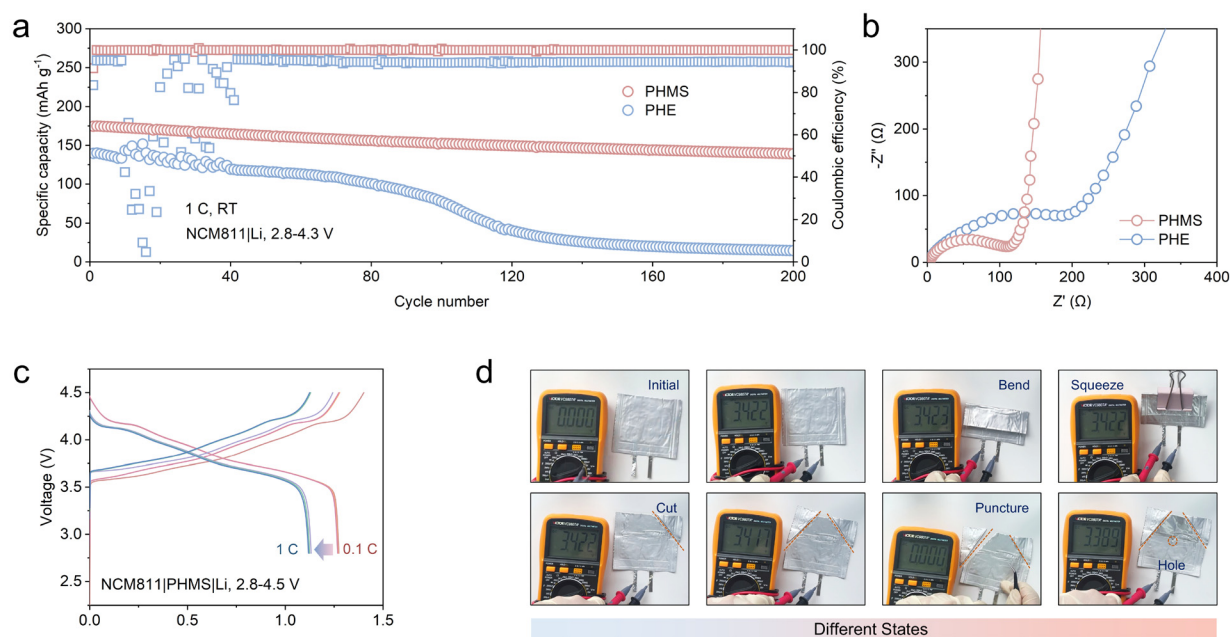
Fig. 6 (a) Cycling performance of NCM811‖Li cells at 1C. (b) EIS profiles of different NCM811‖Li cells. (c) GCD profiles of the PHMS cell within a voltage window of 2.8–4.5 V. (d) Different tests of the LFP|PHMS|Li pouch cell in situations involving severe deformation.

cell maintained its ability to ensure stable open-circuit voltage (Fig. 6d). Notably, under these extreme conditions, there was no occurrence of short-circuit, thereby validating the safety features of the pouch cell. This observation underscores the noteworthy flexibility and robust mechanical properties of PHMS, which proposes a pragmatic solution for the domain of flexible electronics, characterized by its capacity to ensure elevated levels of safety and environmental adaptability.

Conclusions

In conclusion, a sulfur vacancy-enriched MoS_x/PVDF-HFP composite polymer solid-state electrolyte was constructed through a defect engineering strategy. The incorporation of 2D MoS_x fillers has been demonstrated to promote the dissociation of lithium salts, while concurrently constructing a high-throughput ion transport network and inducing the polymer transition to the β-phase, which forms sufficient ion-conducting interfaces inside the electrolyte. This, in turn, significantly enhances the lithium ion transport kinetics, resulting in an increase in the lithium ion transference number to 0.65. Furthermore, the presence of MoS_x fillers resulted in the formation of an SEI comprising a range of inorganic components, thereby facilitating the uniform distribution and deposition of lithium ions, which effectively suppressed the formation of lithium dendrites and provided effective protection for lithium anodes. The LFP|PHMS|Li cell exhibits efficient lithium ion transport and excellent interfacial stability, enabling it to cycle stably at 8500 cycles at a high current density of 8C, with an average capacity decay rate of merely 0.002% per cycle. These

properties underscore the practical application potential of the battery in pouch cells. This work provides a practical and innovative strategy for designing polymer electrolyte materials for ultralong-life solid-state lithium metal batteries.

Experimental

Synthesis of MoS_x nanofillers

The MoS_2 powder and copper nanopowder were subjected to a preliminary grinding treatment, followed by ball milling at 350 rpm for a duration of 2 h under an argon atmosphere. The ball-milled mixture was degassed under an argon atmosphere at 60 °C for 30 min. Thereafter, the mixture was heated to 550 °C at a heating rate of 10 °C min^{-1} and held for 4 h. Subsequently, the mixture was allowed to cool to room temperature. The mixture was washed by repeated centrifugation with nitric acid, distilled water, and ethanol 8 times to remove the residual copper and intermediate products. The precipitate then underwent a drying process at a temperature of 70 °C for 24 h.

Preparation of PHE and PHMS electrolytes

Prior to utilization, the PVDF-HFP particles were subjected to a drying process at a temperature of 60 °C for a duration of 6 h. The preparation of the PHE and PHMS electrolyte membranes involved the employment of the conventional solution casting method. In this method, equal masses of PVDF-HFP particles and LiTFSI were accurately measured, dissolved in DMF, and subjected to heating and stirring at a temperature of 80 °C for 3 h. In the case of the PHMS membrane, MoS_x was incorporated at the initial stage of the process, constituting a mass per-

centage of PVDF-HFP of 15%. Following a drying process at 75 °C for 24 h, the PHE and PHMS electrolytes can be obtained. It is imperative that the electrolytes obtained from the preparation are stored in a glove box and made readily accessible.

Author contributions

Y. Qu contributed to the "conceptualization, methodology, validation, writing – original draft, and writing – review & editing". L. Wang and C. Han contributed to the "conceptualization, data curation, and writing – review & editing". B. Li and W. Song guided the fabrication of the electrolyte membranes. C. Su and W. Jiang explained the results of the theoretical calculations. D. Liu, M. Pei, X. Jin and S. Zhuo reviewed the manuscript and suggested revisions. R. Li presented the original idea. J. Zhang assisted in finding a way to synthesise fillers. X. Jian and F. Hu contributed to the "conceptualization, methodology, funding acquisition, resources, supervision, and writing – review & editing". All authors participated in the experimental work of this study.

Conflicts of interest

The authors declare no conflict of interest.

Data availability

The data supporting this article have been included as part of the supplementary information (SI). For example: detailed descriptions of material characterization techniques, electrochemical testing methods, and theoretical computational methods, along with supplementary data for certain sections of the main text. Supplementary information is available. See DOI: https://doi.org/10.1039/d5eb00152h.

Data are available from the corresponding author upon reasonable request.

Acknowledgements

References

1 M. J. Lee, J. Han, K. Lee, Y. J. Lee, B. G. Kim, K.-N. Jung, B. J. Kim and S. W. Lee, *Nature*, 2022, **601**, 217–222.

2 B. Jin, J. Gao, Y. Zhang and M. Shao, *Smart Mol.*, 2024, **2**, e20230026.

3 Y. Qu, C. Su, L. Wang, B. Li, W. Jiang, R. Li, M. Pei, W. Song, S. Zhuo, X. Jin, D. Liu, X. Jian and F. Hu, *Angew. Chem., Int. Ed.*, 2025, **64**, e202506731.

4 H. Wang, J. Song, K. Zhang, Q. Fang, Y. Zuo, T. Yang, Y. Yang, C. Gao, X. Wang, Q. Pang and D. Xia, *Energy Environ. Sci.*, 2022, **15**, 5149–5158.

5 L. Wang, Y. Qu, C. Su, R. Li, D. Liu, W. Jiang, X. Jin, M. Pei, X. Jian and F. Hu, *Adv. Energy Mater.*, 2025, **15**, 2501185.

6 T. Yu, Y. Liu, H. Li, Y. Sun, S. Guo and H. Zhou, *Chem. Rev.*, 2025, **125**, 3595–3662.

7 Z. Liu, P.-H. Chien, S. Wang, S. Song, M. Lu, S. Chen, S. Xia, J. Liu, Y. Mo and H. Chen, *Nat. Chem.*, 2024, **16**, 1584–1591.

8 Y. Deng, Z. Liang, R. Ma, Y. Zhou, Y. Su, H. Zhong, W. Huang, S. Pan, Y. Luo, Z. Qin, Y. Chen, Z. Gong and Y. Yang, *EES Batteries*, 2025, **1**, 1198–1207.

9 L. Wang, S. Xu, Z. Wang, E. Yang, W. Jiang, S. Zhang, X. Jian and F. Hu, *eScience*, 2023, **3**, 100090.

10 J. Wu, Z. Rao, H. Wang and Y. Huang, *SusMat*, 2022, **2**, 660–678.

11 M. Jacob, K. Wissel and O. Clemens, *Mater. Futures*, 2024, **3**, 012101.

12 J. Li, H. Su, M. Li, J. Xiang, Z. Jiang, X. Wang, X. Xia, C. Gu and J. Tu, *Chem. Eng. J.*, 2022, **431**, 134019.

13 X. Fan, C. Zhong, J. Liu, J. Ding, Y. Deng, X. Han, L. Zhang, W. Hu, D. P. Wilkinson and J. Zhang, *Chem. Rev.*, 2022, **122**, 17155–17239.

14 Q. Wu, M. Fang, S. Jiao, S. Li, S. Zhang, Z. Shen, S. Mao, J. Mao, J. Zhang, Y. Tan, K. Shen, J. Lv, W. Hu, Y. He and Y. Lu, *Nat. Commun.*, 2023, **14**, 6296.

15 W. Lei, H. Li, Y. Tang and H. Shao, *Carbon Energy*, 2022, **4**, 539–575.

16 C. Dai, M. Weng, B. Cai, J. Liu, S. Guo, H. Xu, L. Yao, F. J. Stadler, Z.-M. Li and Y.-F. Huang, *Energy Environ. Sci.*, 2024, **17**, 8243–8253.

17 H. Liang, L. Wang, A. Wang, Y. Song, Y. Wu, Y. Yang and X. He, *Nano-Micro Lett.*, 2023, **15**, 42.

18 C. Fang, K. Huang, J. Zhao, S. Tian, H. Dou and X. Zhang, *Nano Res.*, 2024, **17**, 5251–5260.

19 Y. Liu, X. An, K. Yang, J. Ma, J. Mi, D. Zhang, X. Cheng, Y. Li, Y. Ma, M. Liu, F. Kang and Y.-B. He, *Energy Environ. Sci.*, 2024, **17**, 344–353.

20 L. Nie, J. Zhu, X. Wu, M. Zhang, X. Xiao, R. Gao, X. Wu, Y. Zhu, S. Chen, Z. Han, Y. Yu, S. Wang, S. Ling and G. Zhou, *Adv. Mater.*, 2024, **36**, 2400115.

21 X. Zhang, S. Cheng, C. Fu, G. Yin, L. Wang, Y. Wu and H. Huo, *Nano-Micro Lett.*, 2025, **17**, 2.

22 W. Yang, Y. Liu, X. Sun, Z. He, P. He and H. Zhou, *Angew. Chem., Int. Ed.*, 2024, **63**, e202401428.

23 B. D. Dandena, D.-S. Tsai, S.-H. Wu, W.-N. Su and B. J. Hwang, *EES Batteries*, 2025, **1**, 692–743.

24 Y. Zhu, Z. Lao, M. Zhang, T. Hou, X. Xiao, Z. Piao, G. Lu, Z. Han, R. Gao, L. Nie, X. Wu, Y. Song, C. Ji, J. Wang and G. Zhou, *Nat. Commun.*, 2024, **15**, 3914.

25 Y. Wu, Z. Chen, K. Shi, Y. Wang, X.-A. Li, Z. Zhao, Q. Zhuang, J. Wang and M. Chen, *Energy Environ. Sci.*, 2025, **18**, 2817–2825.

26 Y. Song, H. Qu, Z. Lao, X. Xiao, G. Lu, Y. Song, L. Nie, J. Wang, J. Yang, Y. Zhu and G. Zhou, *Adv. Mater.*, 2025, 2419271.

27 V. B. Mbayachi, L. Liang, B. Zhang, Y. Zhang, G. Zhong, K. Chen and G. Hou, *J. Energy Chem.*, 2025, **110**, 165–175.

28 L. Wang, S. Xu, Z. Song, W. Jiang, S. Zhang, X. Jian and F. Hu, *InfoMat*, 2024, **6**, e12551.

29 S. Hao, Q. Ran, Y. Xiao, L. Li, Y. Ji, J. Liu, Y. C. Yang and X. Liu, *Adv. Mater. Interfaces*, 2022, **9**, 2101486.

30 J. Xu, X.-X. Xue, G. Shao, C. Jing, S. Dai, K. He, P. Jia, S. Wang, Y. Yuan, J. Luo and J. Lu, *Nat. Commun.*, 2023, **14**, 7849.

31 X. Liang, X. Wang, X. Zhang, S. Lin, M. Ji, Q. Liu and M. Wang, *ACS Catal.*, 2024, **14**, 4648–4655.

32 Y. Wu, Z. Chen, Y. Wang, Y. Li, C. Zhang, Y. Zhu, Z. Yue, X. Liu and M. Chen, *J. Energy Chem.*, 2024, **89**, 437–448.

33 Z. Li, I. Sami, J. Yang, J. Li, R. V. Kumar and M. Chhowalla, *Nat. Energy*, 2023, **8**, 84–93.

34 G. Liu, L. Ding, Y. Meng, A. Ali, G. Zuo, X. Meng, K. Chang, O. L. Li and J. Ye, *Carbon Energy*, 2024, **6**, e521.

35 N. Song, J. Ma, Y. Liang, P. Wang, J. Yuan, S. Xiong, X. Li, J. Feng and B. Xi, *Adv. Mater.*, 2025, **37**, 2420588.

36 J. Han, J. Zhou, W. Song, H. Zhang, Z. Wang, K. Liu, Y. Li, W. Zhu, X. Sun and H. Liang, *Appl. Catal., B*, 2024, **359**, 124468.

37 T. Zhao, Z. Song, C. Wu, Y. Li, H. Li, Y. Wei, S. Yao, M. Xiao, M. Zhao and B. Cui, *Smart Mol.*, 2024, **2**, e20240024.

38 B. Li, W. Jiang, Y. Qu, W. Song, X. Jin, M. Pei, S. Zhuo, R. Mao, L. Wang, D. Liu, X. Jian and F. Hu, *Adv. Mater.*, 2025, 2503482.

39 L. Nie, Y. Li, X. Wu, M. Zhang, X. Wu, X. Xiao, R. Gao, Z. Piao, X. Wu, Y. Song, S. Chen, Y. Zhu, Y. Yu, S. Ling, K. Zheng and G. Zhou, *eScience*, 2025, 100395.

40 X. Zhang, T. P. Pollard, S. Tan, N. Zhang, J. Xu, Y. Liu, A. L. Phan, W. Zhang, F. Chen, C. Yang, E. Hu, X.-Q. Yang, O. Borodin and C. Wang, *Nat. Nanotechnol.*, 2025, **20**, 798–806.

41 Z. Niu, Y. Wang, Y. Wang, Y. Wu, Z. Zhao, G. Li, J.-K. Kim, X. Liu, Z. Shen, M. Chen, S. Passerini and Z. Chen, *Energy Storage Mater.*, 2025, **81**, 104492.

42 Q. He, D. Lin, D. Yin, C. Yang, D. Chen and X. Feng, *Smart Mol.*, 2024, **2**, e20240025.

43 B. B. Chen, Y. T. Gao, M. L. Liu, D. W. Li, Q. Liu, Z. Zhao and B. Z. Tang, *Smart Mol.*, 2024, e20240053.

44 Q.-K. Zhang, X.-Q. Zhang, J. Wan, N. Yao, T.-L. Song, J. Xie, L.-P. Hou, M.-Y. Zhou, X. Chen, B.-Q. Li, R. Wen, H.-J. Peng, Q. Zhang and J.-Q. Huang, *Nat. Energy*, 2023, **8**, 725–735.

45 Y. Li, W. Yuan, Z. Hu, Y. Shen, G. Wu, F. Cong, X. Fu, F. Lu, Y. Li, P. Liu, Y. Huang and J. Li, *Adv. Funct. Mater.*, 2025, **35**, 2424763.

46 X. Zhang, Y. Zhang, S. Zhou, J. Dang, C. Wang, W. Wu and J. Wang, *Nano Res.*, 2024, **17**, 5159–5167.

47 T. Zhu, G. Wang, J. Hou, W. Sun, C. Song, Q. Yuan, C. Zhang, X. Lei, Y. Su, M. Chen, Y. Song and J. Zhao, *Adv. Funct. Mater.*, 2025, **35**, 2501870.

48 L. Bi, L. He, Y. Song, Y. Wang, Q. Xie, P. Dong, Y. Zhang, Y. Yao, J. Liao and S. Wang, *Adv. Funct. Mater.*, 2024, **34**, 2311848.

49 S. Lv, X. He, Z. Ji, S. Yang, L. Feng, X. Fu, W. Yang and Y. Wang, *Adv. Energy Mater.*, 2023, **13**, 2302711.